Coastal Engineering 166 (2021) 103868

Contents lists available at ScienceDirect

Coastal Engineering

journal homepage: http://www.elsevier.com/locate/coastaleng

Tidal-flat reclamation aggravates potential risk from storm impacts

Min Zhang [a,b,c], Zhijun Dai [c], Tjeerd J. Bouma [b], Jeremy Bricker [d], Ian Townend [e], Jiahong Wen [a], Tongtiegang Zhao [f], Huayang Cai [g,*]

[a] School of Environmental and Geographical Sciences, Shanghai Normal University, 200234, Shanghai, China
[b] Department of Estuarine and Delta Systems, Royal Netherlands Institute for Sea Research, 4400 AC, Yerseke, the Netherlands
[c] State Key Laboratory of Estuary and Coastal Research, East China Normal University, 200062, Shanghai, China
[d] Department of Hydraulic Engineering, Delft University of Technology, 2628 CN, Delft, the Netherlands
[e] School of Ocean and Earth Sciences, University of Southampton, SO17 1BJ, Southampton, UK
[f] School of Civil Engineering, Sun Yat-sen University, 519082, Zhuhai, China
[g] Southern Marine Science and Engineering Guangdong Laboratory (Zhuhai)/ School of Marine Engineering and Technology, Sun Yat-sen University, 519082, Zhuhai, China

ARTICLE INFO

Keywords:
Reclamations
Extreme value analysis
Storm flooding
Joint probability analysis
Equivalent protection standard

ABSTRACT

A better understanding of how tidal-flat reclamation changes the flood hazard is critical for climate-proofing coastal flood defense design of heavily urbanized areas. Since the 1950s, large-scale reclamation has been performed along the Shanghai coast, China, to fulfill the land demands of city expansion. We now show that the loss of tidal flats may have resulted in harmful impacts of coastal storm flooding. Using the foreshore profiles measured before and after reclamation (i.e., wide vs. narrow tidal flat), we determined the long-term changes in flood risk using a numerical model that combines extreme tidal level and wave overtopping analysis. Results show that wide tidal flats in front of a seawall provide efficient wave damping even during extreme water levels. Reclamation of these tidal flats substantially increased wave heights and correspondingly reduced the return period of a specific storm. As a result, estimates of overtopping are aggravated by more than 80% for the varying return periods examined. It is concluded that the disasters of coastal flooding after the 1997 tidal-flat reclamation in Hangzhou Bay, China are a consequence of both anthropogenic and natural activities. Moreover, our model calculations provide an equation describing the equivalent dike height needed to compensate for the loss of every km tidal flat of a certain elevation, and vice versa. For example, for every km of tidal flat ranging from high marsh to bare tidal flat that is being regained, the dike can be lowered by 0.84 m–0.67 m, when designing for a 1 in 200 years storm event. Overall, we suggest that wide tidal flats are ideally restored in front of dikes, and that when tidal areas are reclaimed, the seawall height is raised as part of the intertidal reclamation procedure. Using such an equivalent protection standard is relevant to designing hybrid flood defense system worldwide.

1. Introduction

Most developing countries with a high population density in Asia, including China, Vietnam, Bangladesh, and the Philippines, primarily rely on seawalls for coastal storm protection (Temmerman et al., 2013; Barbier, 2015). Unfortunately, the natural storm flood mitigation functions of tidal flats (i.e., here refer to both unvegetated mudflat and saltmarshes) have been underappreciated (Möller et al., 2014). Since the middle of the last century, many of these countries have reclaimed large littoral areas for land demands (Bi et al., 2012; Barbier, 2015). The newly reclaimed polders that have been moved further seaward are generally low-lying, and thus highly sensitive to storm impacts. In order to address this issue, China, for instance, had constructed long, hard-engineered defenses of approximately 14,000 km length in total along the 34,000 km-long coastlines to protect its coastal population of roughly 600 million (Liu et al., 2019). The benefit of hard-engineered structures in mitigating economic loss and casualty is universally recognized. However, environmental changes of sea-level rise, land subsidence, and record-breaking extreme storm events are eroding the seawall's protective ability (Temmerman et al., 2013). Maintenance costs are hence expected to rise with time (Liu et al., 2019). Tidal flats are increasingly recognized as "recumbent seawalls", providing

* Corresponding author.
E-mail address: caihy7@mail.sysu.edu.cn (H. Cai).

https://doi.org/10.1016/j.coastaleng.2021.103868
Received 28 April 2020; Received in revised form 4 October 2020; Accepted 13 February 2021
Available online 19 February 2021

long-term protection to the conventional hard-engineered defenses (Willemsen et al., 2020). These natural interfaces with the sea have an inherent resilience against sea-level rise (Kirwan et al., 2016) and hence, in contrast to human-constructed defenses, do not need structural maintenance, and further provide valuable ecosystem services that vertical seawalls do not offer (Reed et al., 2018).

From all intertidal ecosystems, vegetated foreshores are most efficient in attenuating waves due to their highly elevated position in the intertidal zone (Bouma et al., 2014). Therefore, vegetated foreshores, like saltmarshes (Möller et al., 2014) and mangrove forests (Menéndez et al., 2018), are well recognized as ecosystem-based flood protection to reduce storm impacts. Wave mitigation by vegetated foreshores depends

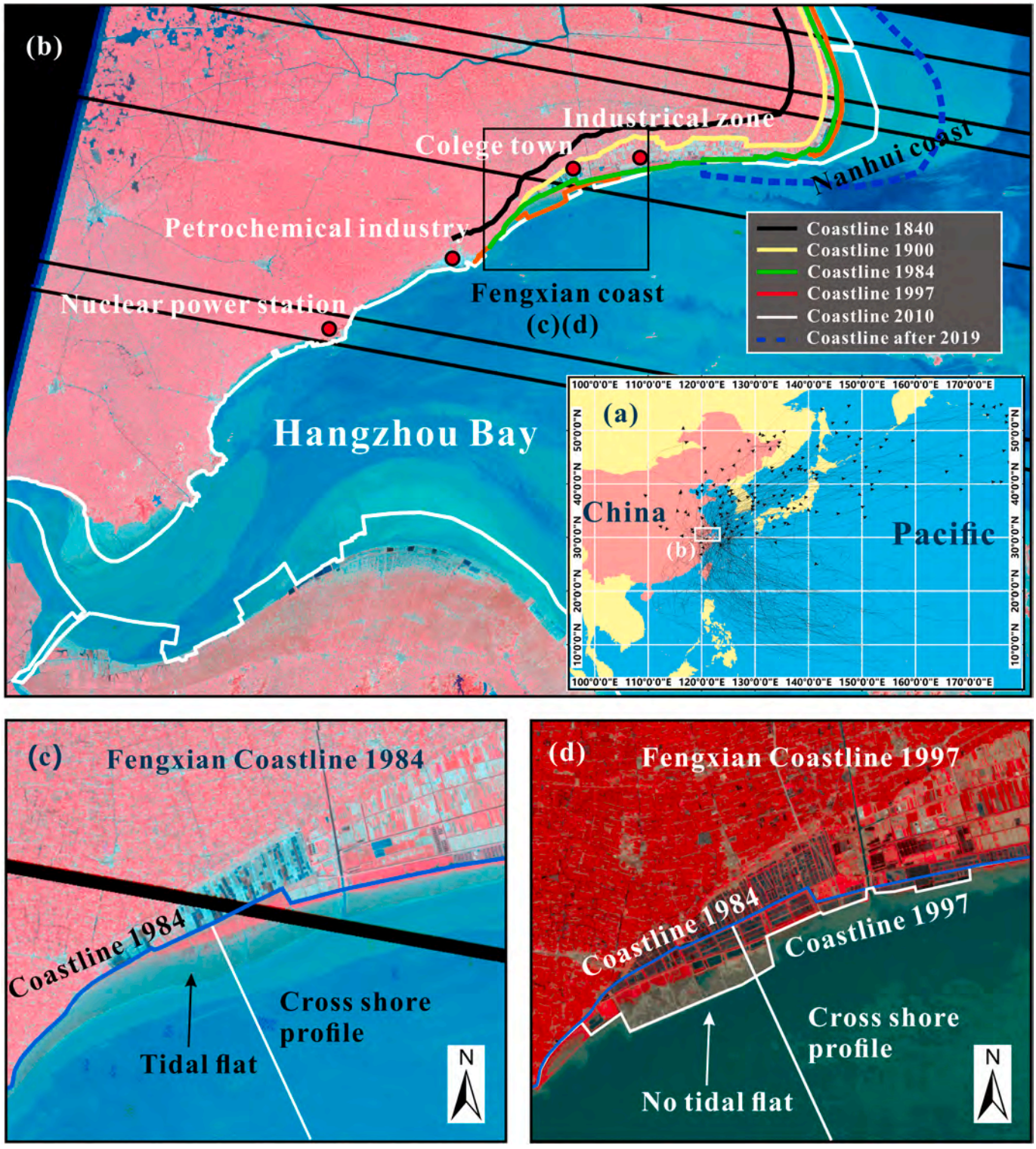

Fig. 1. Archived satellite images showing the history of the study area. (a) The tracks of typhoon events affecting Shanghai during the past 40 years, (b) the historical embankments along the Fengxian Coast and Hangzhou Bay from 1840 to 2010, the area is occupied by existing operational nuclear energy assets, petrochemical industries, and college town, (c, d) detailed map showing the location of seawalls along the Fengxian Coast in the year of 1984 and 1997, the land between the two sets of seawalls denote the reclaimed area.

both on plant traits like shoot stiffness and shoot biomass (Bouma et al., 2005, 2010), stem height, stem diameter, and stem density (Reed et al., 2018), as well as ecosystem traits like marsh width (Willemsen et al., 2020). Even if plant stems break during an extreme storm or are absent, tidal foreshores may still attenuate waves by morphological effects like topographic slopes (Loder et al., 2009; Vuik et al., 2018), bottom friction (Möller et al., 2014), and depth-induced wave breaking (Altomare et al., 2016). Translating this kind of knowledge on wave attenuation to designing hybrid flood defense systems, which consists of a seawall behind a tidal flat, requires numerical models (Vuik et al., 2018). In this study, we aim to integrate the effect of extreme water levels with storm wave run-up into a single long-term modeling effort to quantify how the flood risks of a hybrid flood defense system changes after land reclamation. That is, we model under extreme storm conditions, how wave loading and wave overtopping changes in response to reclamation of tidal areas.

Our study site is the Fengxian Coast, located on the northern bank of Hangzhou Bay, China. Since the 1950s, a large-scale coastal embankment program has been implemented, aiming to improve flood defense and navigation (Xie et al., 2017; Zhang et al., 2018a). At the beginning, embankments only occurred above the high-water level (i.e., high marsh area); however, they were gradually extended onto the intertidal zone (i.e., including low marshes and bare tidal flats), and now reclamation is being performed beyond the low-water level at the −5 m sub-tidal zone to fulfill the increasing land demand (Zhang et al., 2018a) (Fig. 1b). Embankments above the high-water level are believed to be beneficial for flood mitigation (Kundzewicz et al., 2019; Wang et al., 2012). However, little is known about the actual consequences of intertidal reclamation for coastal flood safety and if such measures could reduce or magnify coastal flood risk due to the change of wave run-ups. Moreover, in recent years the Fengxian Coast has changed from being an area of accreting to eroding (Xie et al., 2017), which will lead to an even lower and narrower foreshore at the toe of the seawall in the future. It is reported that the coastal embankments in Bangladesh in the intertidal zone have not always made a positive contribution to flood mitigation (Adnan et al., 2019). Similarly, it is questionable whether the substantial inter- and sub-tidal embankments have reduced flooding risk along the Hangzhou Bay. Therefore, there is a need for a better understanding of the role of tidal flat in helping to mitigate the flood hazard.

In this study, we determine the long-term changes in flood risk using a numerical model that combines extreme tidal levels with wave overtopping analysis, using the foreshore profiles measured before and after reclamation (i.e., wide vs. narrow tidal flat) at the Fengxian Coast. That is, we primarily assess the impacts of reclamation on flood risks by comparing the wave impact on the seawall behind the wide high marsh tidal flat as present in 1984 versus the seawall behind the narrower bare tidal flat as formed after the reclamation that had taken place between 1984 and 1997 (immediately prior to the No. 9711 typhoon event, http://typhoon.zjwater.gov.cn/, accessed on 15 August 2019). These analyses are done on a selected length of the Fengxian Coast, where crucial industries and a college town suffered severe coastal flooding during the No. 9711 typhoon event, resulting in approximately $5.5 billion direct damages (Wang et al., 2012). Particularly, we explored whether reclamations had intensified wave overtopping and increased damage of the No. 9711 event, and to what extent the damage is due to human interventions. A quantitative relationship between the width of intertidal flat (in the horizontal scale) and the height of seawall (in the vertical scale) on equivalent flood protection has been derived to inform the discussion on the non-stationary seawall-foreshore redesign, and how this contributes to or detracts from coastal flood protection.

2. Study area and foreshore bathymetric measurements

The Fengxian Coast is situated on the northern bank of Hangzhou Bay, the largest embayment of China, and on the southern bank of Shanghai Municipality, which hosts the largest economy in China (Fig. 1). It is a region of high importance, having crucial nuclear energy infrastructure, petrochemical industry, and a college town (Fig. 1b). The closest tide gauge station shows that storm surges influencing the Fengxian Coast propagate primarily from Hangzhou Bay, which is a typical funnel-shaped estuary dominated by tides. The semi-diurnal mesotide is approximately in the range of 3–4 m at the entrance of the Fengxian Coast, and increases gradually upstream to reach a maximum of approximately 5–7 m due to the massive bay convergence and broad fetch condition (Xie et al., 2017). This region serves as a location for flood risk studies because of its substantial tidal flat loss and severe coastal storm flooding in history.

Coastal reclamation implemented around Shanghai has a long history (Fig. 1b). Since the 1950s, coastal embankments have been built to improve flood defense and navigation. Unforeseen, the Fengxian Coast has been increasingly flooded, exacerbated by sea defense breaching and overtopping. The most notable example of this is the No. 9711 flooding on 18 August 1997. During this prolonged event, more than 10 km of the seawall was overtopped or breached by a 1 in 200-yr extreme water level coupled with 6 m high waves (see Supplementary Figs. S1 and S2). The flooding extended up to 5 km inland and a maxima depth of 1.2 m due to the low-lying, flat nature of the polders. Hence, the intertidal profile immediately prior to the No. 9711 typhoon event, representing the pre-typhoon conditions, and a much earlier intertidal profile before large-scale reclamations in 1984, are employed to detect the effects of reclamation on flood risk aggravation.

Since the start of reclamation, intertidal profiles had been measured frequently on the Fengxian Coast (Fig. 2). These measurements are part of the Flood Defense Safety led by the Chinese State of Ocean Administration, the governmental subdivision in charge of flood-risk management. A littoral wide intertidal section (slope of approximately 1:700) was present in the 1984 profile, which had been reclaimed in the years 1993, 1995, and 1997, with the polder marching seaward by 2.4 km (Fig. 2). The seawall foundation of 1997 is almost located at the lower margin of the bare tidal flat of 1984, which is in accordance with typical reclamation procedures in China, leaving the toe of the seawall almost uncovered by mud at time prior to the No. 9711 typhoon event. The pre- and post-reclamation profiles are used to determine whether the changes in the tidal flat morphology could influence wave overtopping under storm conditions.

3. Methodology

The investigation into the impacts of intertidal reclamations on aggravated risks from storm surges have been addressed in the following three steps: (1) a framework of numerical models hindcasting tides and waves with improved accuracy is used to downscale the offshore sea states to those at the toe of the seawall; (2) the outputs of tidal levels (*TLs*) and significant wave heights (*SWHs*) of independent storms are used for the extreme value analysis, and the resulted marginal distributions are further fed into the joint probability model for overtopping estimation using the method by Tuan and Oumeraci (2010); and (3) the different effects under the adopted bathymetry profiles before and after reclamation in 1984 and 1997 are compared.

3.1. Wave and surge models

The long-term tides and storm surges are generated using the coupled TELEMAC-TOMAWAC modules to capture the wave-current interactions (Zhang et al., 2018a). The full, two-dimensional primitive equations of Navier Stokes and the balance equations of wave action density spectrum for both deep and shallow water physics are solved using the finite difference method (Janin et al., 1992). The computational domain, shown in Fig. 3a, encompasses the entire Yangtze Estuary and Hangzhou Bay and a portion of the nearby coastal regions. The domain is extended to ensure a sufficient fetch for wave simulation, so that the development of storm swells in the deep ocean and the

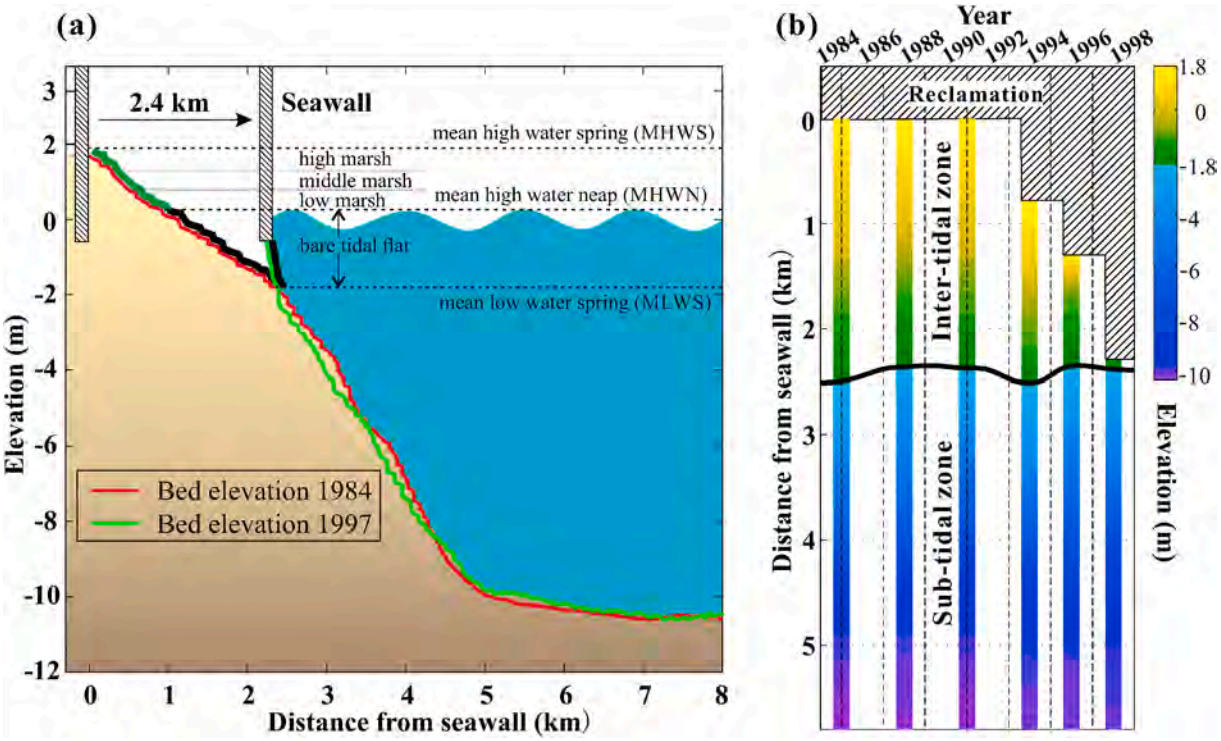

Fig. 2. Morphodynamics of the cross-shore profiles. (a) Schematic representation of seawall-foreshore change with marks indicating ocean parameters of mean high water spring (MHWS), mean low water spring (MLWS), mean high water neap (MHWN), and foreshore division of high marsh (1.3–1.8 m), middle marsh (0.8–1.3 m), low marsh (0.3–0.8 m) and bare tidal flat (−1.8–0.3 m). The location of cross-shore profiles measurements are shown in Fig. 1c and d. (b) Detailed bed elevation measurements between 1984 and 1997, including the hard boundary of seawall toe position and the position of MLWS (the solid black line of −1.8 m). The change of seawall position denotes the reclamation procedures occurring in 1993, 1995, and 1997. The distance between seawall and MLWS is the intertidal zone, where marshes are believed to grow above 0.3 m.

propagating with tides to the nearshores are captured (Zhang et al., 2018a). An appropriate simulation of tides and swells propagation to nearshore is crucial for a high-accuracy simulation of wave runups at the toe of seawall.

In order to obtain the long-term nearshore waves, two sets of local wave models embedded with 1984 and 1997 bathymetries, covering the Fengxian Coast (Fig. 3b and c), are configured with TOMAWAC module (EDF, 2011), and cascading to the upper-level Yangtze-Hangzhou Bay model. For the local wind-wave simulations, wave energy dissipation mechanisms, including bottom friction, wave breaking, and white capping, are triggered. JONSWAP-type bottom friction and depth-induced wave breaking are used. The spectral frequency is discretized by 30 frequencies, with a minimum frequency of 0.055 Hz, increasing equidistantly at an interval of 0.03 Hz. The bathymetries are also delineated with unstructured irregular triangular meshes, with the edges aligned with the 1984 and 1997 coastlines, respectively. Both local wave models are run with the same meteorological and oceanic forces, i.e., at the sea surface boundary, temporally variable and spatially uniform 10 m height wind force, obtained from field measurements is used; at the lateral sea boundary, water levels and wave spectra extracted from the regional domain model are interpolated onto the seaward boundary of the TOMAWAC model to consider swell and wave propagation from the deep ocean.

After the bathymetries of the meshes are corrected to the consistent datum of Huanghai 1985, the depths are modified to account for sea-level rise (SLR), which has been shown to have some influences on nearshore wind-wave generation (Chini and Stansby, 2012). The present simulation assumed a linear SLR rate of 3.5 mm/yr over the past 40 years. Early estimates of the SLR for the region of the East China Sea ranged from 2.1 to 2.5 mm/yr (Shi et al., 2000), whereas more recent studies (post-1990), based on a satellite altimeter, suggested a higher rate of 5–6 mm/yr (Chini and Stansby, 2012).

3.2. Data sources used to set-up model

To drive the large-scale Yangtze-Hangzhou Bay model, long-term astronomical tide and atmosphere (e.g., wind and pressure) data for the past 40 years are derived through the TOPEX/POSEIDON global ocean tidal model (TPXO, http://volkov.oce.orst.edu/tides, accessed on 15 August 2019) calculation and European Centre for Medium-Range Weather Forecasts (ECMWF, http://www.ecmwf.int/, accessed on 15 August 2019) reanalysis, respectively. The tidal amplitudes at the ocean boundary are forced with harmonic compositing of eight primary, two long-period, and three non-linear constituents provided by TPXO (Zhang et al., 2018a). The temporal and spatial resolution for the wind and pressure field derived from ECMWF is 3 h and 12.5 km, respectively. Such high-resolution data are a proper source to drive the ocean model over a large area because the forces imposed on the Yangtze-Hangzhou Bay model encompass distinct pressure gradients and heat capacity contrasts from the typhoon center to the margin, resulting in rapidly varying wind and pressure fields (Dee et al., 2011).

In addition to the meteorological data from ECMWF, a 40-yr uninterrupted wind data recorded every 6 h between 1979 and 2018 by the Fengxian Observation Station (E121.45°, N30.93°, established in 1961) are collected from the Shanghai Meteorological Bureau, and is presented in Fig. 4d, e, f, and g. Seasonal variability in wind directions is clearly observed. They are used to force both sets of local models, i.e., the morphologies of 1984 and 1997, respectively. By setting a high wind threshold of 15 m/s, the peak-over-threshold analysis (Méndez et al., 2006) performed on the wind data above the given threshold identified 270 typhoon events that had hit Shanghai during the past 40 years (Fig. 1a).

Other observation data used in the model include seabed bathymetries and hydrologic station records. The archived daily river discharge measured at the Datong station (1981–2018) is imposed on the river

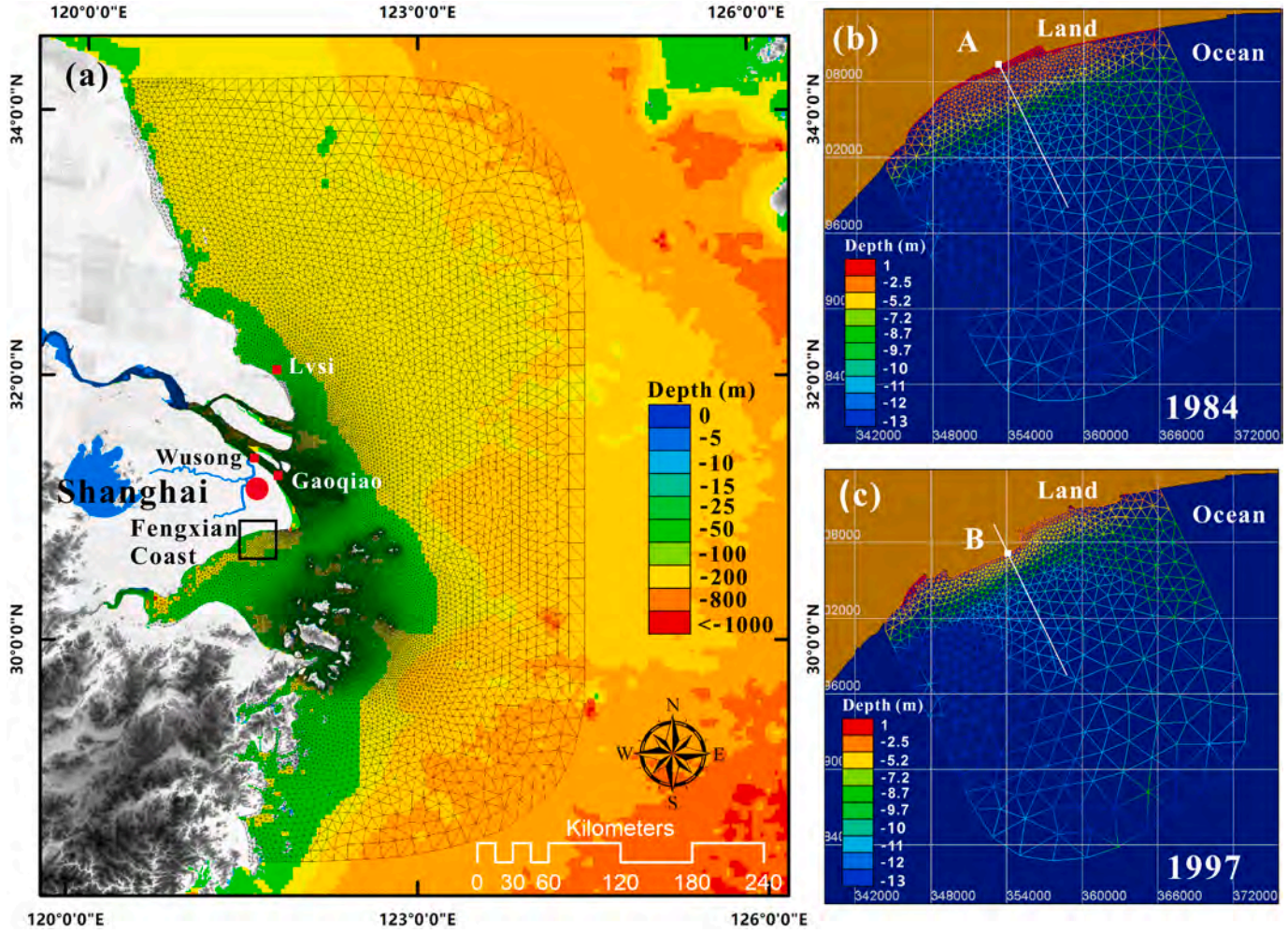

Fig. 3. Maps of the modeling domain. (a) Regional domain of Yangtze-Hangzhou Bay model for the tide and swell simulation, and (b, c) local domain of the Fengxian Coast model for the wave simulation with the applied morphology profile of 1984 and 1997 bathymetry, respectively. The solid white lines indicate the location of cross-shore profiles the same as shown in Fig. 1c and d.

boundary to capture the signal of abrupt releases of discharges from the Changjiang River catchment. The depth information of the mesh is defined by the amalgamation of heterogeneous databases, including the General Bathymetric Charts of the Oceans (GEBCO, https://www.gebco.net, accessed on 15 August 2019) dataset, covering the continental shelf area, the 2007 and 2008 navigation charts collected for the Yangtze River channel, the river mouth and the bar area. These data are all interpolated and corrected relative to the mean sea level of the Huanghai 1985 datum in ArcGIS software.

3.3. Model performance

Because the hindcast of the 40 years storm tide simulation is substantial, only selected periods are used for simulation-measurement comparisons. Four periods of simulated and observed water levels at tidal stations of Lvsi, Gaoqio, and Wusong (see their locations in Fig. 3a) affected by devastating typhoons are illustrated in Fig. 5. These storms were reported to have caused the most substantial economic losses for Shanghai over the past half-century (Wang et al., 2012). Typhoon 7910 in August 1979 and Typhoon 8114 in August 1981 are used for calibration, while Typhoon 0012 in August 2000 and Typhoon 0509 in August 2005 are used for validation (see Fig. 4d, e, f, and g for corresponding wind forces). In order to quantify the model's performance, the correlation coefficients of root-mean-square error (RMSE), mean-normalized bias (B_{MN}), and skill value between simulations and measurements are evaluated, as presented in Fig. 5. The RMSE, B_{MN}, and skill values of the measurements are fairly consistent with the simulations with means of 0.38 m, 0.09, and 0.99, respectively. The maximum RMSE and B_{MN} values are 0.42 m and −0.11 (negative means underprediction), respectively, at the Wusong station for Typhoon 0509, but the model's skill value reached 0.98, indicating the reasonable accuracy of the model performance.

Based on the above-mentioned model calibration and validation procedures, some common modeling parameters are determined, including the hydrodynamic time step of 180 s, the horizontal diffusion viscosity coefficient of 0.1 $kgm^{-1}s^{-1}$. A linearly increasing wind friction coefficient (i.e., from 0.00125 for 7 m/s wind speed to 0.0025 for 25 m/s wind speed) is applied in order to resolve the error of underestimated peak typhoon wind speed from ECMWF (Dee et al., 2011). A Nikuradse bottom frictional coefficient of $N = 0.05 \pm 0.02$ m is used, based on the Manning values typically used for tidal marshes in typhoon conditions (Möller et al., 2014; Vuik et al., 2016). For the bare tidal flats, $N = 0.001$ m is applied. For detailed descriptions of the model's configuration and calibration around the Yangtze Estuary and Hangzhou Bay, readers can refer to our previous publications, such as Zhang et al. (2018a; 2019).

3.4. Extreme value analysis

The hourly-simulated *TL*s and *SWH*s during typhoon periods are extracted and subjected to extreme value analysis by fitting to the

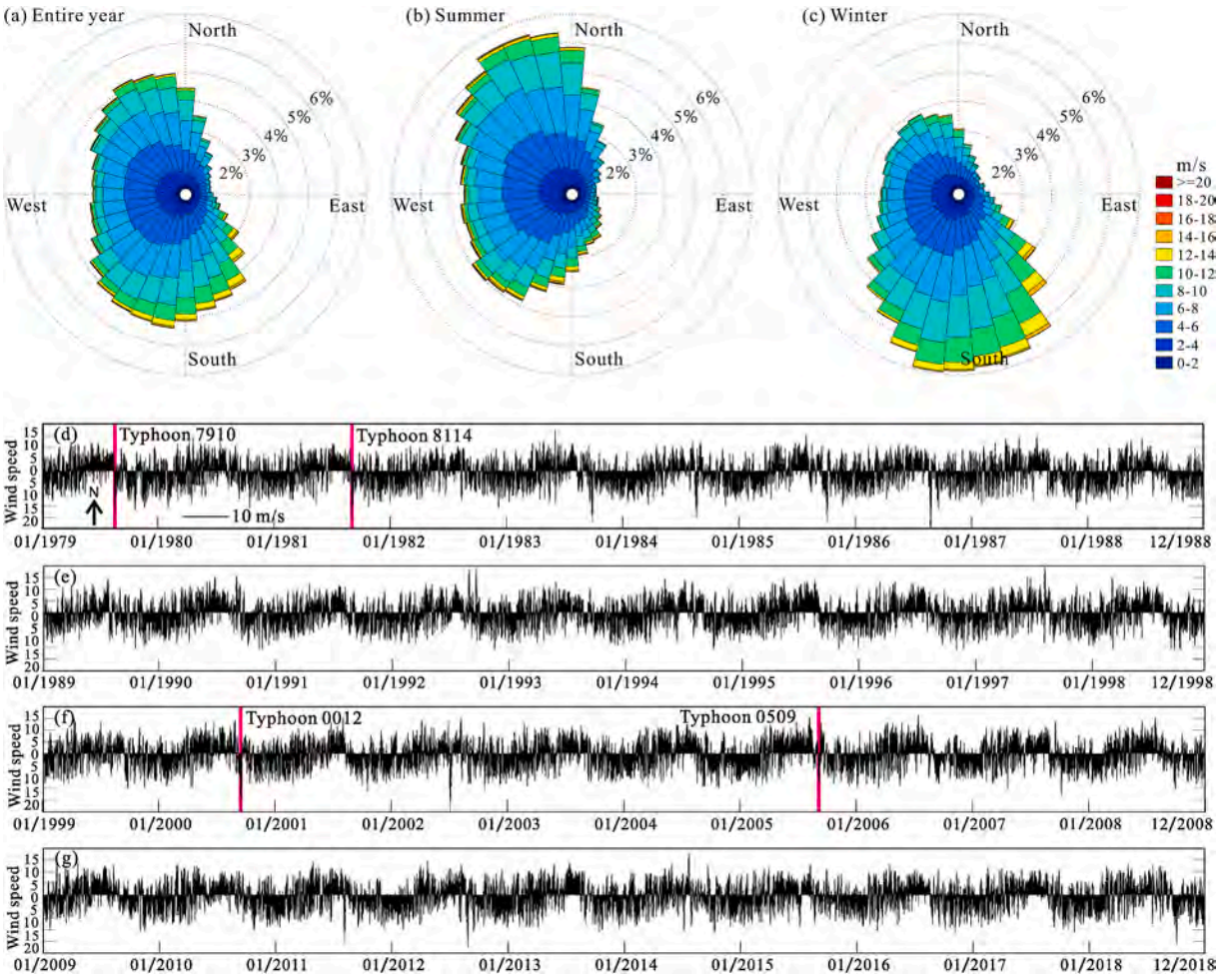

Fig. 4. Meteorological data of wind observed uninterrupted during 1979–2018 recorded by the Fengxian Observation Station (E121.45°, N30.93°). (a, b, c) The wind rose of the entire year, the summer (May–October) and winter (November–April) periods. (d, e, f, g) The 6-hourly recorded wind magnitudes and directions from 1979 to 2018.

appropriate marginal distributions, i.e., Normal, Gamma, Weibull, and GEV (generalized extreme value) (Niroomandi et al., 2018). Statistics of the Chi-Square test for the theoretical distributions indicating the best choice is GEV distribution (see Supplementary Table S1). Firstly, the stationarity GEV distribution is used to model the different behavior of extremes with three parameters $\theta = (\mu, \varepsilon, \sigma)$, representing the location, shape, and scale parameters, respectively. The cumulative distribution function of stationarity GEV is given by (Chini and Stansby, 2012):

$$F(z) = \exp\left\{ -\left[1 + \varepsilon\left(\frac{z-\mu}{\sigma}\right)\right]^{-1/\varepsilon} \right\} \varepsilon\left(\frac{\mu - z}{\sigma}\right) < 1 \quad (1)$$

where z is the variable of *TLs* or *SWHs*. The Mann-Kendall and likelihood ratio estimation are then performed to test the time-series trends (Cheng et al., 2014). If the trend is significant, a linear function of parameter μ is included in order to take into account non-stationarity:

$$\mu = \mu_0 + \mu_1 t \quad (2)$$

where t is the time in years, μ_0 is a constant and μ_1 is the linear trend. In this way, GEV is extended with four parameters $\theta = (\mu_0, \mu_1, \varepsilon, \sigma)$ to predict the future extremal levels in a non-stationarity form, e.g., t = 0 for 1979, t = 40 for 2019 and t = 121 for 2100. A framework combining Differential Evolution Markov Chain (DE-MC) and Bayesian inference (Cheng et al., 2014) is used to obtain the uncertainty bounds (95% quantile) of the ensemble of estimated return levels, taking into account the uncertainty in all model parameters for both stationarity (μ, ε, σ) and non-stationarity ($\mu_0, \mu_1, \varepsilon$, σ). Finally, the return period (T), representing an event that has a $1/T$ chance of occurrence in any given year, is estimated by the following formula:

$$T(z) = \frac{1}{1 - F(z)} \quad (3)$$

For each set of bathymetries, the return periods of *TLs*, $F(w)$, and *SWHs*, $F(s)$, are estimated by Eq. (3), denoted by $T(w)$ and $T(s)$, respectively.

One primary concern of the extreme value analysis lies in the application of monthly maxima data, thus ignoring other essential values during the month (Niroomandi et al., 2018). However, most typhoons hit Shanghai only in summer, i.e., June to October (Wang et al., 2012, 2019). In this study, the peak-over-threshold (*POT*) method, combined with the block maxima, is used to reduce this limitation by identifying independent storms (Méndez et al., 2006). The wind speeds above a threshold of 15 m/s and a successive time span maximum of 3 days (regarded as a block) are used to guarantee the independency between consecutive storms. The block maxima method is then used to extract the independent maxima for each storm. These criteria enable the division of the entire data into non-overlapping periods of individual storms as blocks and the selection of the maximum value from each block; therefore, it is deemed adequate to perform extreme value analysis. As a result, there are samples of 270 extreme values used to fit the GEV distribution for the long-term 40-yr study.

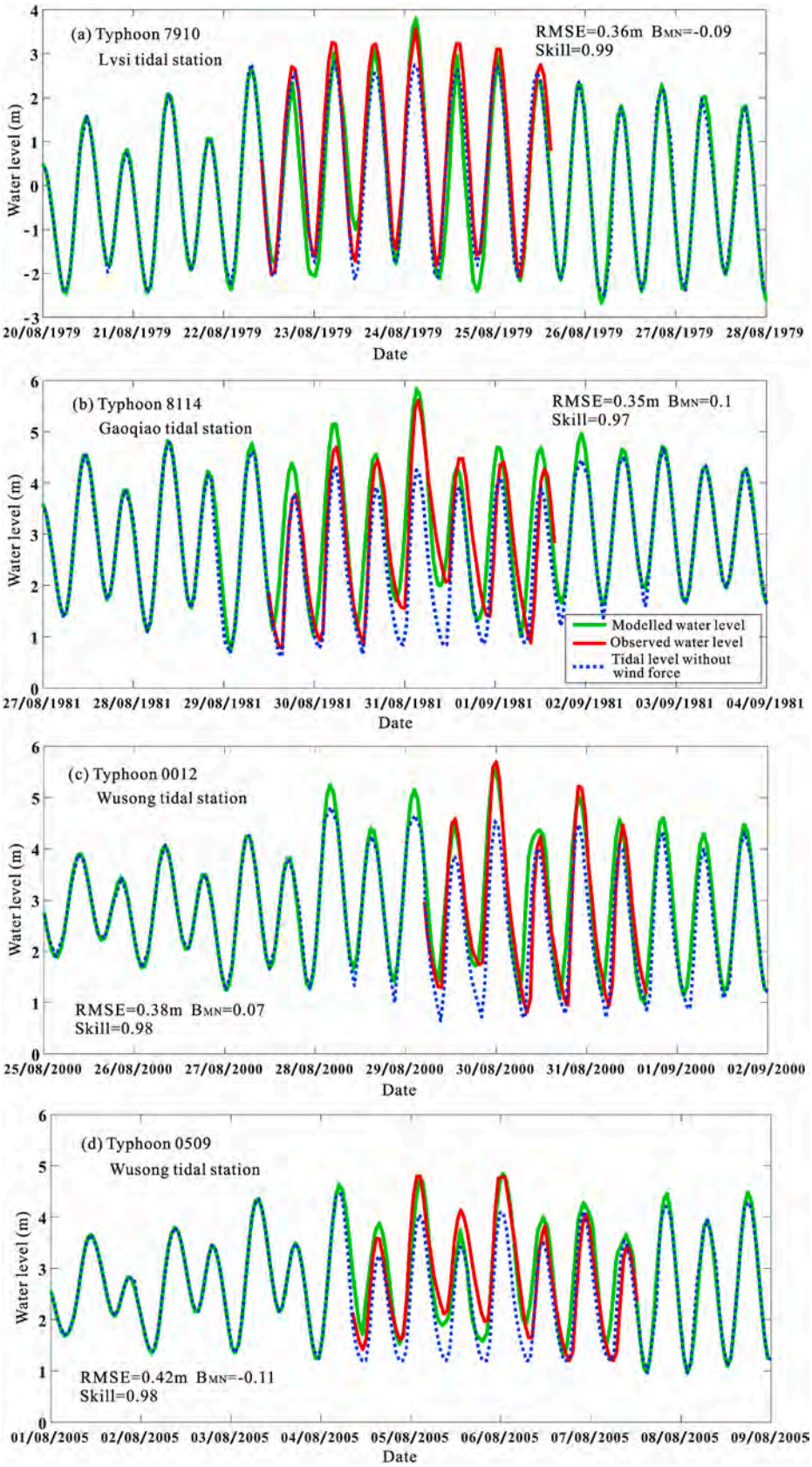

Fig. 5. The comparison of modeled (green line) and observed (red line) water levels at tidal stations of Lvsi, Gaoqio, and Wusong (see Fig. 3a) during typical typhoons of (a) 7910, (b) 8114, (c) 0012, and (d) 0509. The blue dot lines show the tidal level without considering the typhoon wind forces. (For interpretation of the references to colour in this figure legend, the reader is referred to the Web version of this article.)

3.5. Copulas joint probability analysis

Since *TLs* and *SWHs* are rarely statistically independent, the joint probability of multivariate analysis (i.e., the Copulas) is used to calculate the overtopping occurrence by determining the correlations between *TLs* and *SWHs* (Chini and Stansby, 2012). The Copula function is actually a class of function that connects joint distributions and marginal distributions (Lin-Ye et al., 2016, 2017). Based on the definition of Copula (Rigby and Stasinopoulos, 2005), the joint distribution of the hydrological variable pair (x_1^t, x_2^t) can be described by non-stationary Copula with an explanatory variable of time *t*:

$$F\left(x_1^t, x_2^t\right) = C\left[u_1\left(x_1^t \middle| \lambda_1^t\right), u_2\left(x_2^t \middle| \lambda_2^t\right) \middle| \lambda_c^t\right] \tag{4}$$

where $F(x_1^t, x_2^t)$ is the joint cumulative distribution function (*CDF*) of *TLs* and *SWHs*, C represents the non-stationary Copula function, u_1 and u_2 are the non-stationary cumulative marginal distribution of *TLs* and *SWHs*, with λ_1^t and λ_2^t the time-varying marginal distribution parameters. If the time-dependent parameters λ_1^t, λ_2^t and λ_c^t are set to constants, then Eq. (4) is converted to stationary Copula. More information about the non-stationary Copula can be found in Lin-Ye et al. (2016; 2017).

The implementation of the time-dependent Copula is powered by the Generalized Additive Model in Location, Scale and Shape (GAMLSS) package to measure the partial dependence structure of the parameters (Rigby and Stasinopoulos, 2005). The first step is to implement the non-stationary extreme value analysis for each variable and select an appropriate marginal distribution, as presented in 3.4. Then, the Archimedean Copula function is used to measure the dependence between *TLs* and *SWHs* based on the well-documented Copula family methods, i.e., the Gaussian, Clayton, Frank, and Gumbel (Rigby and Stasinopoulos, 2005; Lin-Ye et al., 2016). The Akaike Information Criterion (AIC) values for different Copulas fitted to *TLs* and *SWHs* for the periods before and after reclamation suggest that the Gaussian method is the most suitable (see the Supplementary Table S2).The joint return period $T(w, s)$ is formulated as:

$$T(w,s) = \frac{1}{1 - F(w) - F(s) + F(w,s)} \tag{5}$$

where $F(w)$, $F(s)$, and $F(w,s)$ are the cumulative distribution probability of *TLs*, *SWHs*, and their joint distribution probability, respectively. A significant number of observations are required to achieve a robust fit of the joint probability distribution, and here, we used long-term simulations for this purpose.

4. Results

4.1. Return levels of stationary and non-stationary estimations

In order to examine the changes of extreme tidal levels (*TLs*) and significant wave heights (*SWHs*) due to reclamations, a detailed analysis of all independent storms is provided using the plots of probability distributions (Fig. 6a–c). A more explicit comparison of the change of return levels versus the corresponding return periods under both stationary (ignoring the observed trend, Fig. 6d–f) and non-stationary assumptions (Fig. 6g-o) are also presented. The initial goodness-of-fit of the GEV model is assessed using Quantile-Quantile (Q-Q) plots of the observed and empirical values, which are presented in Fig. S3 of the Supplementary. Overall, the stationary posterior probability bounds of simulations do not encompass all the *TLs* points, especially for the points at the beginning (Fig. 6d), indicating that the assumption of stationary model is not met, considering the trend of continuous sea-level rise. Whereas, the envelope of *SWHs* encloses the points of empirical return levels under both the stationary (Fig. 6e and f) and non-stationary (Fig. 6 h-i) assumptions, since the trend of *SWHs* is mostly related to the intensifying of typhoon storms, which is only assessed based on a relatively short period of observation (e.g., 1978–2019). Nonetheless, if the observed linear trend continues, the future predicted return levels would be inadvertently underestimated under the stationary assumption. For example, considering a 100-yr-return level, it is 2.77 m (stationary), 2.85 m (non-stationary of 2060), and 2.92 m (non-stationary of 2100) for 1997 *SWHs*; it is 3.11 m (stationary), 3.18 m (non-stationary of 2060), and 3.22 m (non-stationary of 2100) for *TLs*, respectively. These results indicate that an unrepresentative assumption of stationary underlying distribution would underestimate future extreme return levels.

It is shown that the changes in the hourly *TLs* are not significant, even considering the fact of reclamations between 1984 and 1997 (see Fig. S4 in the Supplementary Material). The same number of *TL* histograms of independent storms, shown in Fig. 6a, are observed distributing between the range of 1.8 m and 3.2 m under both 1984 and 1997 conditions, i.e., both median (~2.42 m) and extreme values (99.5 percentile) of the *TLs* distribution are unchanged after reclamation on Fengxian Coast. In contrast, the *SWHs* have increased profoundly after reclamation (Fig. 6b and c). In particular, the median of *SWHs* has tripled (i.e., 0.43 m and 1.15 m for 1984 and 1997, respectively), while a 145% increase in the 99.5 percentile is also observed when compared with the case before reclamation, demonstrating a profound shift towards higher values of both median and extreme wave height after reclamation on Fengxian Coast. In addition, the return levels of 1997 *SWHs* after reclamation (Fig. 6f, i) are much higher than those before reclamation in 1984 (Fig. 6e, h) under both stationary and non-stationary assumptions. For example, the return levels of *SWHs* corresponding to 1-yr, 5-yr, 10-yr, 20-yr, 50-yr, 100-yr and 200-yr on Fengxian Coast are increased by 1.31 (1.28–1.36) m, 1.64 (1.60–1.72) m, 1.75 (1.69–1.85) m, 1.83 (1.76–1.96) m, 1.93 (1.83–2.08) m, 1.98 (1.88–2.16) m and 2.02 (1.91–2.22) m, respectively, which corresponds to an increase of *SWHs* by more than twofold when compared with the case before reclamation, as presented in Supplementary Table S3. Consequently, reclamations of the high marshes on Fengxian Coast had a substantial amplification of *SWHs* when compared with a minor change in *TLs*.

4.2. Risk estimation based on joint probability models

Based on Copulas joint probability analysis, we compared the difference in the joint dependence structure of *TLs* and *SWHs* between the pre- and post-reclamation periods. For the Fengxian Coast that was modified by reclamations in 1997, both occurrence probabilities (Fig. 7a) and return periods (Fig. 7b) of the given *TLs* and *SWHs* events tend to be more substantial for the post-reclamation period, particularly for those values around the 45° line (Fig. 7a and b). Regarding the *TLs*-*SWHs* joint return periods (Fig. 7b), different combinations of *TLs* and *SWHs* can have the same joint probability of occurrence, although the overtopping volume and flood hazard may be different. We also notice that, for the various return periods examined (Fig. 7b), there are no obvious changes in the dependence structure between the two periods when *SWHs* are lower than 0.4 m (i.e., the impacts of reclamations on the change of return levels are limited for the ordinary low wind-wave conditions). On the contrary, for strong wind and wave conditions higher than 0.4 m (especially for typhoons), the isolines of return levels show more significant and progressive increases with the decrease in *TLs* during the post-reclamation periods (Fig. 7b). These observations suggest that depth-induced wave breaking during storms is absent after reclamation. Consequently, the situation may become very dangerous for some typhoons even when coincidence with medium-low *TL* stages.

The change of risk is also shown using the scatter plot of hourly *TLs* and associated *SWHs*, which differs enormously between pre- and post-reclamation periods (Fig. 7c and d). Though the upper right corner is influential in overtopping, it is worth noting that the minimum *TLs* elevation is 0.85 m before reclamation due to the limit of tidal flat elevation; the maximum wave heights show a linear increase (with a slope of 0.45) with *TLs*, further demonstrating the importance of water

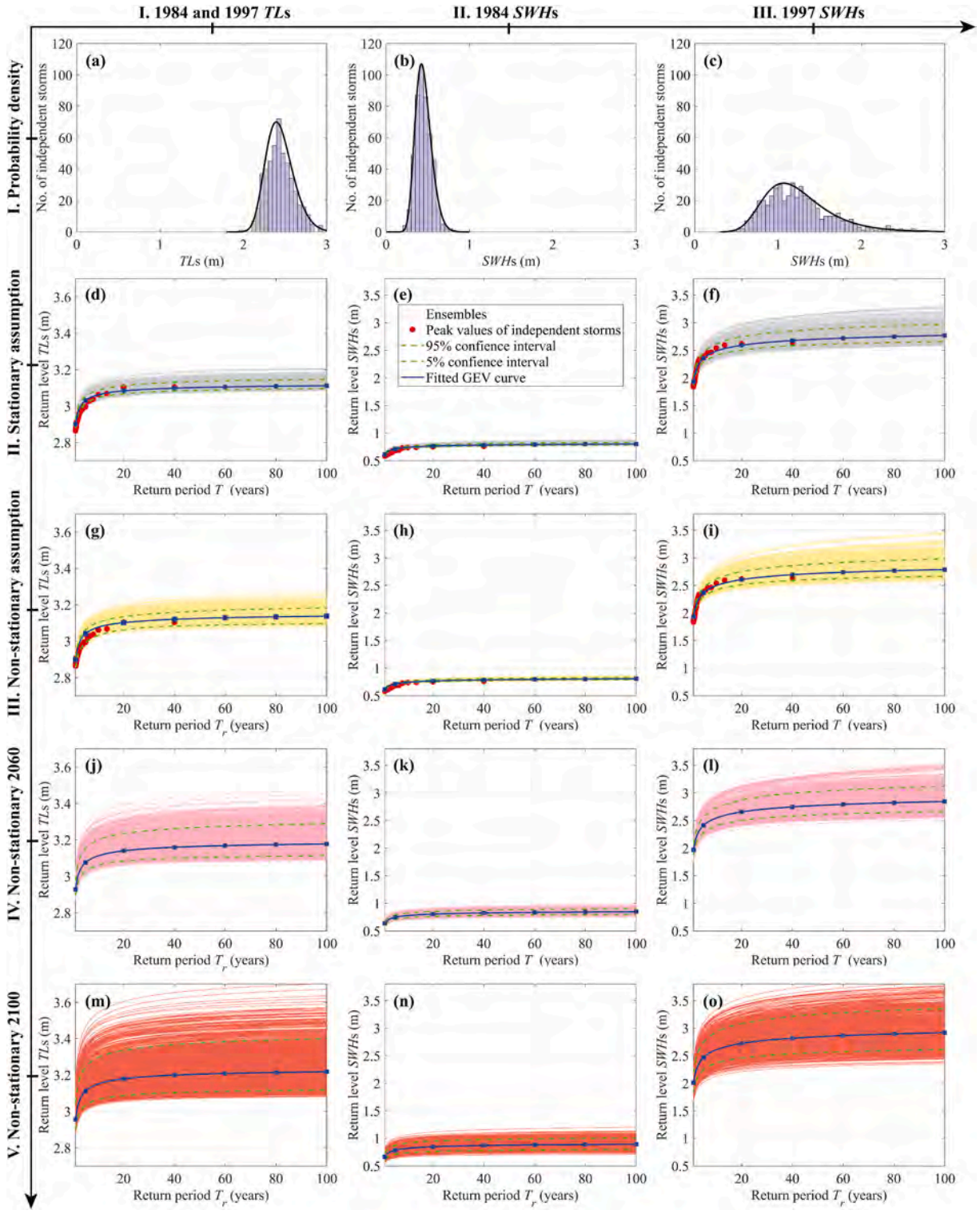

Fig. 6. Diagnostic plot of independent storms for the probability density (1st row) and return levels vs. return periods with fitted GEV (generalized extreme value) curve (2nd - 5th row). Ensembles are used to provide the range of posterior probability bands and the confidence intervals (e.g., 5% and 95% quantiles). The 1st column is the tidal levels (*TLs*) for both 1984 and 1997 tidal flat conditions, the 2nd and 3rd columns are the significant wave heights (*SWHs*) under 1984 and 1997 tidal flat condition, respectively. Stationary assumption: showing the return levels under the stationary distribution function; Non-stationary assumption: exhibiting the non-stationary return levels for the observation period 1979–2018; Non-stationary 2060: displaying the predicted non-stationary return levels for 40 years beyond observations (e.g., 2019–2060); Non-stationary 2100: displaying the predicted non-stationary return levels for 80 years beyond observations (e.g., 2060–2100).

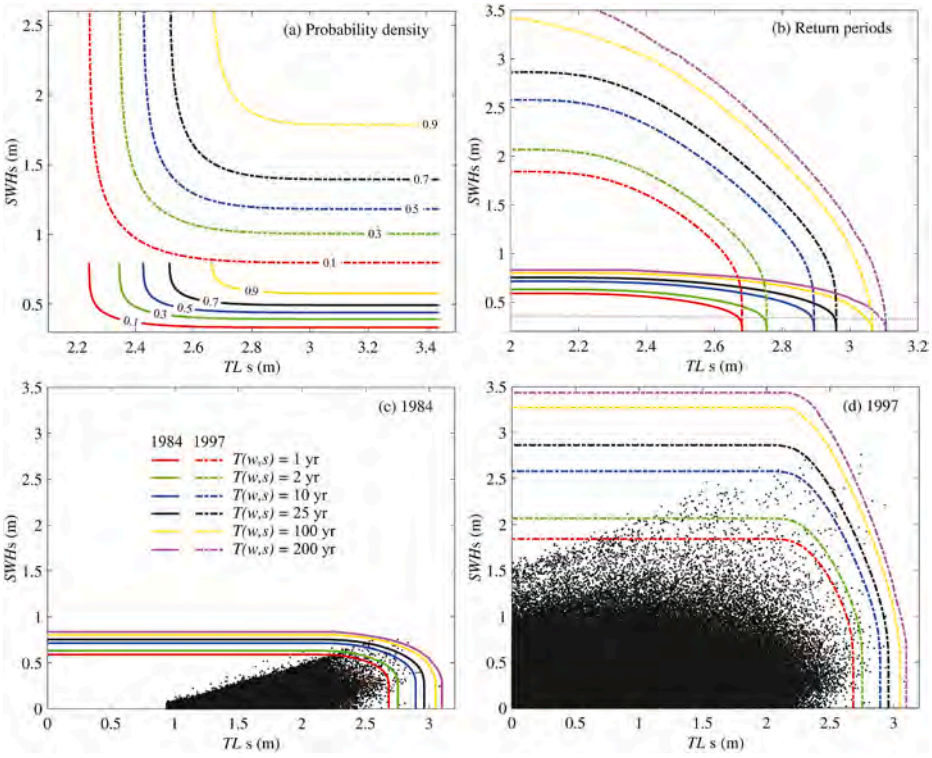

Fig. 7. Joint cumulative probability curves and joint return period curves for nearshore *TLs* and *SWHs*. (a, b) Comparison of joint cumulative probability $F(w,s)$ curves and joint return period $T(w,s)$ curves before and after reclamation; (c, d) the scatter plot of hourly *TLs*-*SWHs* for the past 40 years, and the comparison with the associated joint return period curves under the 1984 and 1997 intertidal profiles, respectively.

depth on wave breaking before reclamation. As a response, China has developed various design standards for sea defense, depending on the properties being protected. For example, nuclear energy assets are designed to be resilient to events less than 0.005%, but a typical design tolerance for urban areas is a 0.5% event. For an extensive verification of this result, six joint probability isolines of 100%, 50%, 10%, 4%, 1%, and 0.5% are considered (Fig. 7c and d), historically known as 1 in 1, 2, 10, 25, 100 and 200-yr-return period events. Assuming the coastal defense in Shanghai is designed to withstand a 1 in 200-yr-return period event, our analyses reveal that for *TLs* higher than 2.8 m, for instance, to prevent wave overtopping, a dike needs to be able to withstand *SWHs* higher than 0.8 m and 2.4 m for the periods pre- and post-reclamation, respectively. Notably, points located outside of the 200-yr-return period, in Fig. 7d, are instantaneous extreme overtopping during Typhoon 9711.

4.3. The conversion from tidal-flat reclamation to seawall heightening on equivalent flood protection

The most common strategy to combat wave overtopping after reclamation of tidal-flat areas is seawall heightening. However, seawall heightening can be difficult if the intertidal subsoil is too soft to support a heavy dike. Alternatively, restoring the wide tidal flat by human interventions provides a reliable way to reduce seawall overtopping risks. Here, we introduce an equivalent conversion formula (*ECF*, m/km) to explore the relationships between seawall heightening (vertical scale, in m) and tidal flat restoration (horizontal scale, in km) that provides the same standard of flood protection for storms of a specific return period. Firstly, we assume stationary return levels of an unbounded lifetime of exceedance probability. Thus, reducing the marshes on Fengxian Coast by every km width of tidal flat is estimated to increase of *SWHs* by $ECF = 0.0536 \cdot \ln(T_r) + 0.5839$ m, with return periods T_r varying from 1 to 200 years (see Fig. 8a and Table S3 in the Supplementary Material), which is equivalent to the heightening in seawall crest level to achieve the same protection ability, and vice versa. The tidal flat loss occurred in 1984 is due to the reclamations of high marshes with the elevation of 1.8 m (at the toe of seawall). For a general derivation, *ECFs* of the reclamations of middle marshes (elevation of 1.3 m), low marshes (elevation of 0.8 m), and bare tidal flats (elevation of 0.3 m) are also modeled and presented in Fig. 8b, c and d, respectively. By summarizing the above four different marsh cases, a more general equation of *ECF* as a function of tidal flat elevation (E) placed in front of the seawall can be obtained by a regression model, leading to steady $ECF = 0.0493 \cdot \ln(T_r) + 0.1342\ E + 0.3618$ m under stationary assumption.

Considering the fact that the exceedance probability varies over time (Fig. 6), stationary estimation assuming an unbounded lifetime of facilities will potentially underestimate the risks compared with the actual lifecycle analysis. Consequently, a 50-yr seawall lifecycle and 100-yr seawall lifecycle, termed as effective *ECFs* are presented in Fig. 8, which can be considered more practical estimates of future *ECFs*. For example, the *ECF* corresponding to 100-yr-return period, reclamation of high marsh is estimated to be 0.82 (0.75–0.89) m, 0.83 (0.77–0.93) m and 0.85 (0.78–0.98) m for the unbounded lifetime, 50-yr lifecycle and 100-yr lifecycle, respectively (Fig. 8a). The effective *ECFs* can be considered as a low risk (more conservative) estimation of actual lifecycle analysis by taking the 95 percentiles of the $\mu(t)$ values into extrapolation from historical observation to future prediction. Thus, the concept of Design Life Level quantifying the probability of exceeding a fixed threshold is extended to be a time-varying exceedance probability to provide a more reliable saltmarsh design. Based on the non-stationary assumption the steady *ECF* equation is revised, leading to $ECF_{50} = 0.0494 \cdot \ln(T_r) + 0.1341\ E + 0.3618$ m and $ECF_{100} = 0.0495 \cdot \ln(T_r) + 0.1341\ E + 0.3618$ m considering the seawall lifecycle of 50 years and 100 years, respectively. The performance of effective *ECFs* are shown in Supplementary Fig. S5, where we observe a good correspondence between modeled and observed results with R^2 being 0.97.

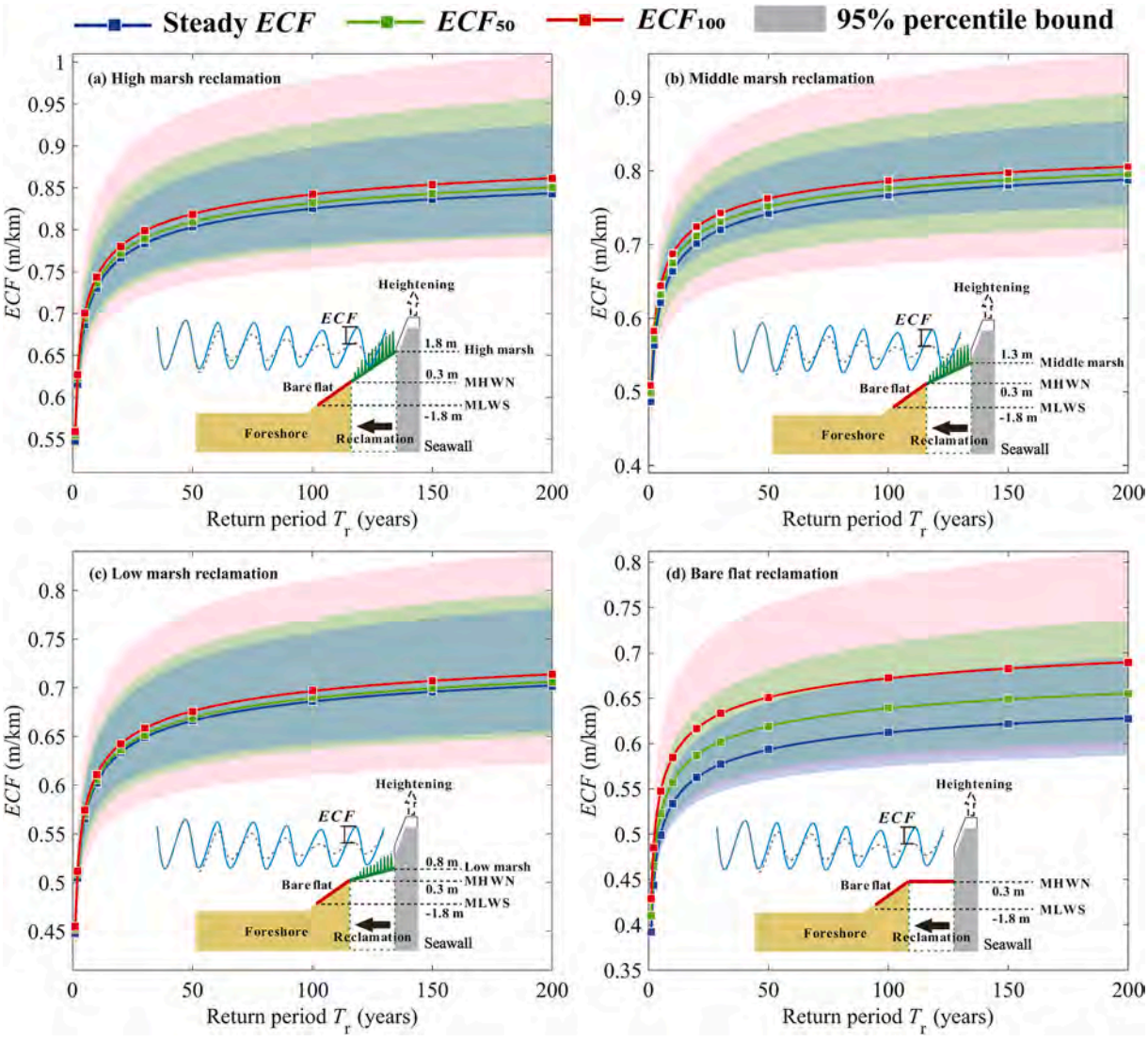

Fig. 8. The equivalent conversion relationship (*ECF*) on flood protection from the heightening of seawall (in m) against 1 km reclamation of (a) the 1984 tidal flat of high marsh (1.8 m) on Fengxian Coast, considering steady *ECF* (the steady condition assuming an unbounded seawall lifetime), and effective *ECF* considering the seawall lifecycle of 50 years (ECF_{50}) and 100 years (ECF_{100}), respectively. For a general prediction, *ECF* for reclamations of (b) the middle marsh with the mudflat elevation of 1.3 m, (c) the low marsh with the mudflat elevation of 0.8 m, and (d) the bare tidal flat with the mudflat elevation of 0.3 m are also presented, with the shade showing the 95% percentile bound. (For interpretation of the references to colour in this figure legend, the reader is referred to the Web version of this article.)

4.4. Changes of occurrence probability after reclamation

Following wave amplification at the toe of seawall during post-reclamations, the return periods are decreased; thus, the exceedance probability of wave overtopping for a given *SWHs* is also changed. Fig. 9 shows how the 10–200 yr return periods of *SWHs* in 1984 are modified by a series of reclamations in 1997. For instance, for various elevations of tidal flat that are reclaimed assuming no improvement in seawall defense, 100–200 yr return periods of *SWHs* would occur at least once in 25–35 yr for reclamations of every km width of bare tidal flat (0.3 m), at least once in 5 yr for low marshes (0.8 m), and at least once in 2 yr for middle marshes (1.3 m) or high marshes (1.8 m), respectively. Reclamations, therefore, increase the extreme magnitude of *SWHs* on the Fengxian Coast and correspondingly reduce the return period of a specific magnitude computed with the foreshore before reclamation. In other words, an exceedance probability of 0.005–0.01 (representative of an event that has the chance of occurrence in any given year) will increase to around 0.03–0.04 after reclamation of bare tidal flat, and even increase to above 0.5 for the reclamation of middle or high marshes. Thus, extreme coastal flood disasters such as the No. 9711 typhoon event would become more frequent under the present condition than those existing before the reclamation of the tidal flats on the Fengxian Coast.

4.5. The contribution of human-induced and natural changes to overtopping risks

For any given storm wave run-ups (i.e., defined by a combination of hourly *TLs* and *SWHs* in Fig. 7c and d under 1984 and 1997 bathymetry, respectively) and seawall height (i.e., defined by the return levels for 1997 in Fig. 7d), we derived the total time-integrated potential exceedance volume (i.e., wave overtopping volume assuming seawall heights are set at the derived return levels) for 1984 and 1997, respectively (Fig. 10). The deeper water at the toe of seawall due to tidal-flat loss caused by land reclamation increases the wave height and the potential exceedance volume as a consequence. It is shown that the increase in overtopping is more than 80% between the pre- and post-reclamation periods for the various return periods examined. Therefore, it is concluded that reclamation is a highly significant contributory factor to the storm overtopping of historical events such as Typhoon No. 9711, and it is estimated that human-induced and natural changes had

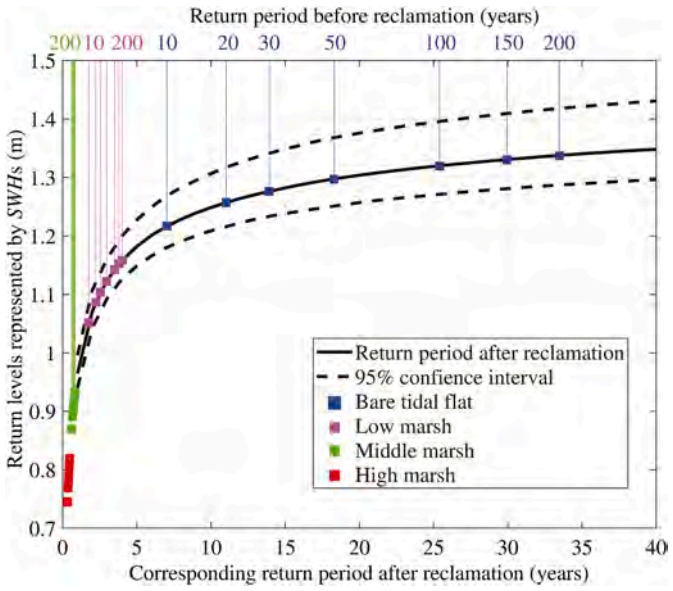

Fig. 9. Changes in return periods computed before and after reclamation of every km width of tidal marshes, where red dots, green dots, pink dots, and blue dots represent the return periods before reclamation of the high marsh, middle marsh, low marsh, and bare tidal flat, respectively. The black curve represents the return period vs. return level after reclamation, with 95% percentiles shown by dashes. (For interpretation of the references to colour in this figure legend, the reader is referred to the Web version of this article.)

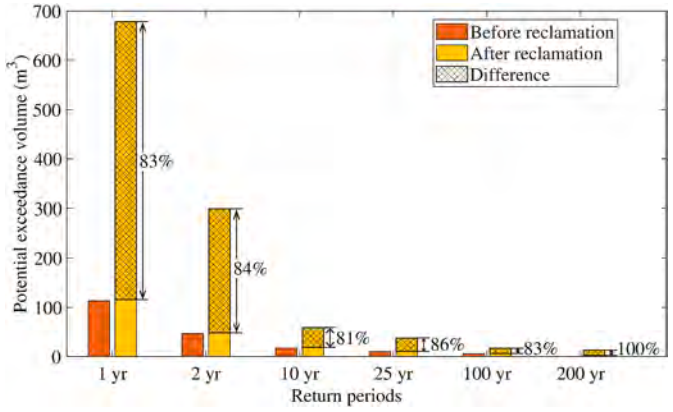

Fig. 10. Comparison of potential exceedance volume before and after reclamation, assuming seawall is set to the heights of 1 in 1, 2, 10, 25, 100, and 200-yr-return levels computed with 1997 narrow intertidal condition.

contributed approximately 80% and 20% to storm overtopping of typhoon disasters, respectively, during post reclamations. To avert such an event, the seawall height would need to have been raised as part of the intertidal reclamation procedure, in line with the increase in wave conditions suggested by the *ECF*, to produce an equivalent protection standard.

4.6. Wave attenuation by tidal flat

Tidal flat forms an interface between land and sea, which dissipates wave energy, thereby reducing the impact of storms on the coastal area. Hindcasting the ten most influential storms occurred over the last 40 years (i.e., Typhoon 7910, 8114, 9711, 0012, 0509, 0608, 0813, 1211, 1323, and 1416), based on pre- and post-reclamation bathymetries, demonstrates that the shallow tidal flats indeed strongly attenuate wave propagation towards shore (Fig. 11). Before reclamation, the *SWHs* are

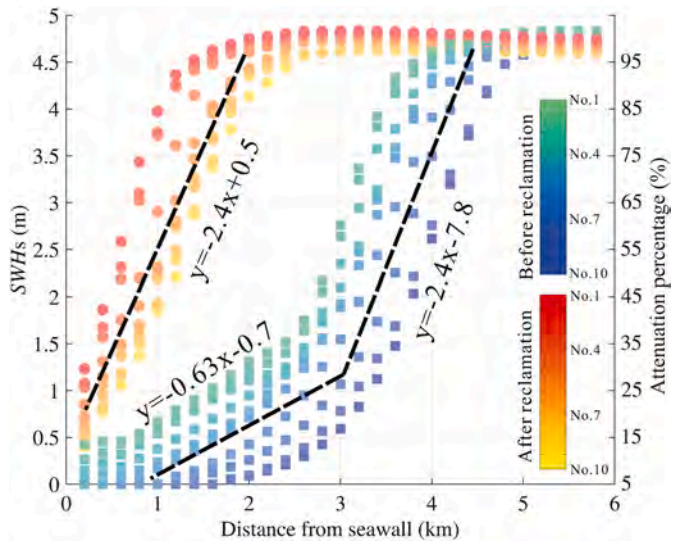

Fig. 11. Trend analysis of wave height reduction and attenuation ratio for the ten largest storms during the past 40 years. Colorbars denote the conditions before and after reclamation.

initially decreased by an average of 2.4 m per km for a sudden morphology transition from the deep bay (4.5 km offshore at around −9 m depth) to the shallow coast (see Figs. 2a and 11), and is further attenuated by 1.2 m when the waves passed over the additional 3 km wide tidal flat, transition from the depth of −3.5 m to the toe of the original seawall in 1984. The additional (secondary) wave attenuation after the major wave dissipation is due to the existence of extensive high-marsh tidal flat. However, after reclamation, the high-marsh tidal flat is completely lost, so as the secondary wave attenuation as a consequence. The *SWHs* are monotonically reduced from a maximum height of approximately 4.5 m to the height of 1 m over a distance of 1.5 km (i.e., equivalent to a linear slope of 2.4 m per km). Therefore, wave reductions are strongly related to width and elevation of the intertidal flat.

5. Discussion

Although vegetated foreshore is demonstrated to provide storm protection (Möller et al., 2014; Reed et al., 2018), it is proved challenging to quantify the evidence of the impacts of the tidal flat reclamation program on coastal flood risks due to the facts that (i) intertidal reclamations are always accompanied with procedures of seawall strengthening and heightening, (ii) tidal flat morphology consisting of a sediment body in front of the dike is continuously evolving especially shortly after reclamation, and (iii) it is difficult to establish to what the extent and severity the overtopping may have occurred had the intertidal reclamation not been implemented. We address these challenges by (i) analyzing the potential exceedance probability assuming the seawall height set to the obtained return levels rather than using the actual seawall height, (ii) modeling the past extreme events to identify the impacts of reclamations, and (iii) comparing the possibility of overtopping that could have occurred had the reclamation not been implemented. Specifically, a cascade of numerical models has been designed to transfer the regional surge propagation to local wave overtopping. This framework is coupled with a time-dependent extreme value analysis to investigate the long-term influence of tidal flat reclamations.

5.1. The impacts of coastal reclamations on risk aggravating

Reclamation of the tidal flat profoundly influenced the coastal geomorphology, and thus, increased wave run-ups (Loder et al., 2009; Liu et al., 2019). The derivation of *ECF*s demonstrates that a lower intertidal elevation with a steep gradient profile after reclamation could allow

more substantial overtopping than the foreshore before reclamation, and this conversion relationship positively correlated with foreshore elevations and slopes at the toe of the seawall (Salauddin and Pearson, 2019). In addition, the increase in wave height due to tidal flat reclamation could potentially increase direct wave attacks on the otherwise protected seawall, exacerbating damages and increasing the need for reinforcement (Loder et al., 2009; Vuik et al., 2016). Erosion of soil at the toe of the seawall after reclamation may also occur during storm events, increasing the need for armoring the intertidal morphology (Loder et al., 2009). Recently, breakwaters had been placed at the wet-side of seawall around Fengxian Coast to protect against wave run-ups (see Supplementary Fig. S6). This is consistent with the results of Chini and Stansby (2012) for coastlines not protected by nearshore sandbanks, while for coasts with fast accretion, reclamation has a potentially lower impact on the amplification of nearshore waves and therefore overtopping risks (e.g., in the vicinity of Nanhui on the southeast coast of Shanghai, see Fig. 1b) (Zhang et al., 2018b).

Intertidal conservations, on the other hand, can effectively mitigate overtopping by limiting the transfer of offshore wind-waves to coastal wave run-ups (Bi et al., 2012; Vuik et al., 2016). Möller et al. (1999; 2014) presented quantitative evidences for wave attenuation by coastal saltmarshes over a wide range of tidal and meteorological conditions both numerically and experimentally. The increases in bottom friction and bulk drag force by vegetation are the primary reasons for wave attenuation over the saltmarshes (Möller et al., 1999; Vuik et al., 2016). Here, the effect of the bulk drag force is neglected to provide a more conservative estimation. It is predicted that restore in every km width of tidal flat corresponds to approximate the asymptote of $ECF = 0.0493 \cdot \ln(T_r) + 0.1342\ E + 0.3618$ m rise of seawall height on the equivalent flood protection (Fig. 8). Nevertheless, changes in sedimentation affect intertidal conservation, and this may vary over space and time, e.g., for rapidly regression area near the mouth of Ganges estuary and Yellow River estuary (Adnan et al., 2019; Temmerman et al., 2013; Barbier, 2015), or transgression foreshores near Pearl River estuary and Hong estuary (Kundzewicz et al., 2019; Liu et al., 2019), but delivers a consistent role of tidal flats for coastal protection on the contribution to wave attenuation. Therefore, it is suggested that wide tidal flat should be restored in front of dikes via human interventions in the face of rising sea levels and intensified storms (Kirwan et al., 2016). Otherwise, the seawall height would need to have been raised as part of the intertidal reclamation procedure (Liu et al., 2019), in line with the increase in wave conditions suggested by the equivalent conversion relationship.

5.2. The sensitivity of SWHs dynamics to wind force

In order to quantitatively explain the reason of overtopping risk variation after reclamation, a sensitivity test of the wave propagation towards the toe of seawall is compared with varying wind forces under both 1984 and 1997 bathymetries (Fig. 12). Obviously, the wave rose shows three-fivefold larger the magnitude of *SWHs* after reclamation than that before reclamation, which should have schematically demonstrated the causes of the increase in extreme wave height. A significant change in *SWHs* is also observed when the wind speed changes ranging 5–20 m/s and wind direction changes ranging 0–360°. The results are consistent with those from Tuan and Oumeraci (2010) and the manual of EurOtop (2018), which suggests that *SWHs* increase with the increase in wind speed but decrease with the incidence of wind shifts away from the angle normal to the coastline. Therefore, except for wind speed, wind incidence is also a critical parameter impacting wave heights at the toe of the seawall because wave run-ups on the outer slope of the seawall are governed by both wave periods and directions (Loder et al., 2009; Altomare et al., 2016; EurOtop, 2018).

In addition, the shoreward winds are shown to be more influential than offshore winds on wave generation (Fig. 12). Since the prevailing seasonal winds in eastern China vary in the southeast-northwest direction during summer and winter, respectively (Fig. 4b and c, see also Zhang et al., 2018a), indicating higher wind-waves during summer (the typhoon season) than those during winter near Fengxian Coast (Zhang et al., 2018a). Notably, before reclamation in 1984, the wide and shallow intertidal is very efficient at reducing *SWHs* when the wind angle is normal to the coastline at high wind speed. A maximum *SWHs* reduction rate of 35% is observed when the wind speed is 20 m/s and the wind incidence is normal to the coastline. Therefore, it is predictable that before reclamation in 1984, the wide and shallow tidal flats could protect the coastline by reducing the most severe wind-waves during the worst typhoon conditions. Nevertheless, this function is totally lost after reclamation, which generally agrees with the wave attenuating measurements reported in other literatures (Loder et al., 2009; Vuik et al., 2016; Willemsen et al., 2020).

5.3. Contribution to coastal flood defense designs

Coastal defense design has long relied on stationary return levels, assuming the constant occurrence probability of extreme event over time (Altomare et al., 2016; Rootzén and Katz, 2013). However, substantial evidences show that the climate is non-stationary, so as the associated hydrologic extremes, possibly due to both anthropogenic and natural changes (Barbier, 2015; Cheng et al., 2014). Therefore, the concept of Design Life Level, introduced by Rootzén and Katz (2013), quantifies the probability of exceeding a fixed threshold during the design life of seawall should be improved to meet the non-stationary purpose. We assume the location parameter (μ) of the underlying

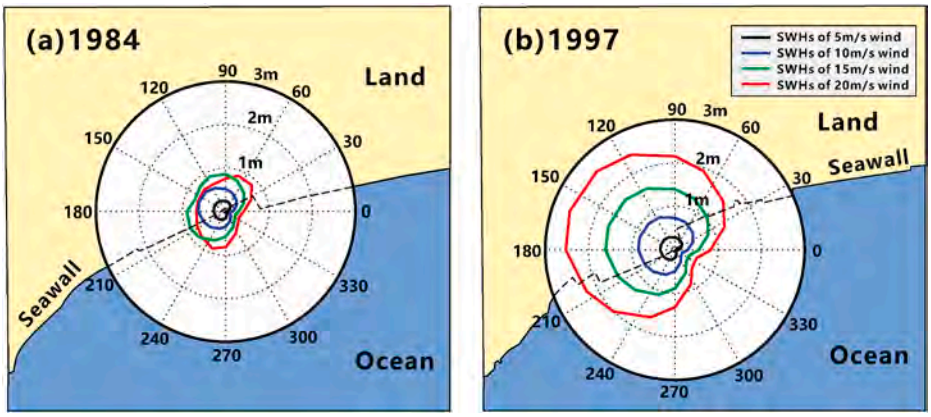

Fig. 12. Sensitivity tests of wave propagation approaching the toe of the seawall. (a) Directional wave rose under the applied morphological profiles of 1984 and (b) under the 1997 tidal flat profile. The magnitude of *SWHs* changes following the change of both wind direction (0°–360°) and wind speed (5–20 m/s). The sectors indicate the wave directions, or the direction towards which the wind vector is directed.

distribution function is time-dependent (Rigby and Stasinopoulos, 2005; Lin-Ye et al., 2016, 2017) and hence, the extreme value of the distribution varies with time (Cheng et al., 2014). A visual inspection indicates an upward trend for *TLs* and *SWHs* during observations (Fig. 13), which is confirmed with the Mann-Kendall trend test at the 5% significance level. Fig. 13 shows how the running return level varies with the time covariate used in the linear trend assumption (Eq. (2)). This means that the return levels vary with time to keep the occurrence probability of an extremal event constant, such that a specific return level used for all years have the same risk.

On Fengxian Coast, both *TLs* and *SWHs* show linear running return levels increase over time (Fig. 13), which confirms the aggravation of future overtopping of a specific return level, assuming no improvement in the seawall defense. On the other hand, *TLs* show little change after reclamation while *SWHs* are almost tripled; thus, extreme typhoon events will become more frequent than those existing before reclamation. The *ECF* demonstrating the relationship between tidal flat loss and seawall heightening, illustrated in Fig. 8, provides suitable guidance for seawall redesign. The minor changes in *TLs* demonstrate that reclamations in a local-scale at nearshore imposed a limited influence on the large-scale tidal state, which is mainly controlled by astronomical tide and swell propagation from the open sea (Loder et al., 2009; Niroomandi et al., 2018; Zhang et al., 2018a). It is worth noting that extrapolating the historical trends linearly into the future implies that the characteristics of the past trend continues following an inertia (linear function) without constraints, which might be not realistic (Méndez et al., 2006; Cheng et al., 2014). For time-varying prediction of the probability of exceedance instead of simply linear extrapolating result from historical trends, one must rely on other tools like numerical modeling, as the dynamical Yangtze-Hangzhou Bay simulations performed in this study. In principle, long-term and reliable future boundary conditions of atmosphere (e.g., typhoons) and hydrology (e.g., SLRs) should be addressed appropriately of the first importance. Therefore, care should be taken in the future earth prediction, especially for the long-term climate changes (Shi et al., 2000; Dee et al., 2011).

5.4. Implications for coastal reclamation adaptations

Large-scale reclamations and embankments have been implemented in the coastal zone of Shanghai for more than half a century (Xie et al., 2017). The reclamation procedure is still underway and looks set to continue (Zhang et al., 2019). The most straightforward engineering approach in response to the aggravating of coastal flood hazards due to tidal flat loss is seawall heightening. However, seawalls and dikes only provide flood protection to a given hazard severity (EurOtop, 2018; Tuan and Oumeraci, 2010). These structures are typically costly and may exacerbate flooding due to the build-up of wave run-ups (Altomare et al., 2016; Kundzewicz et al., 2019). Moreover, the base subsidence will further lower the seawall's protection standard if maintenance is inadequate, and therefore, potentially aggravate the overtopping risks (Temmerman et al., 2013). There are reported examples worldwide of protection failure by traditional hard engineering defenses, e.g., North Sea storm surge flood in 1953, Typhoon Winnie flood in 1997, Hurricane Katrina flood in 2005, Storm Xynthia flood in 2010, and most recently, Typhoon Mangkhut flood in 2018. Alternative adaptation strategies, such as vegetated foreshore, sediment nourishment, and groynes should be considered part of the Flood Defense Safety Plan by building the hybrid seawall-foreshore system to maximize the coastal resilience functions.

Generally, wide foreshore restorations in front of seawall via human interventions are both for the immediate wave run-up reduction (Reed et al., 2018; Vuik et al., 2019) and in anticipation of elevated future risks due to SLR (Temmerman et al., 2013). On the other hand, saltmarshes on the foreshores are a gift of nature, and they provide valuable ecosystem services that hard seawalls do not (Bouma et al., 2010; Reed et al., 2018). The comparison of overtopping changes and *ECF* estimation before and after reclamation reported in this study should help to demonstrate the importance of tidal flats on flood mitigation and to establish plans to adapt coastal zone against flood hazards by helping to optimize protection design and maximize the benefit of flood management. Nevertheless, the usability of such a nature-based solution should fit in with the surrounding physical environment (Adnan et al., 2019;

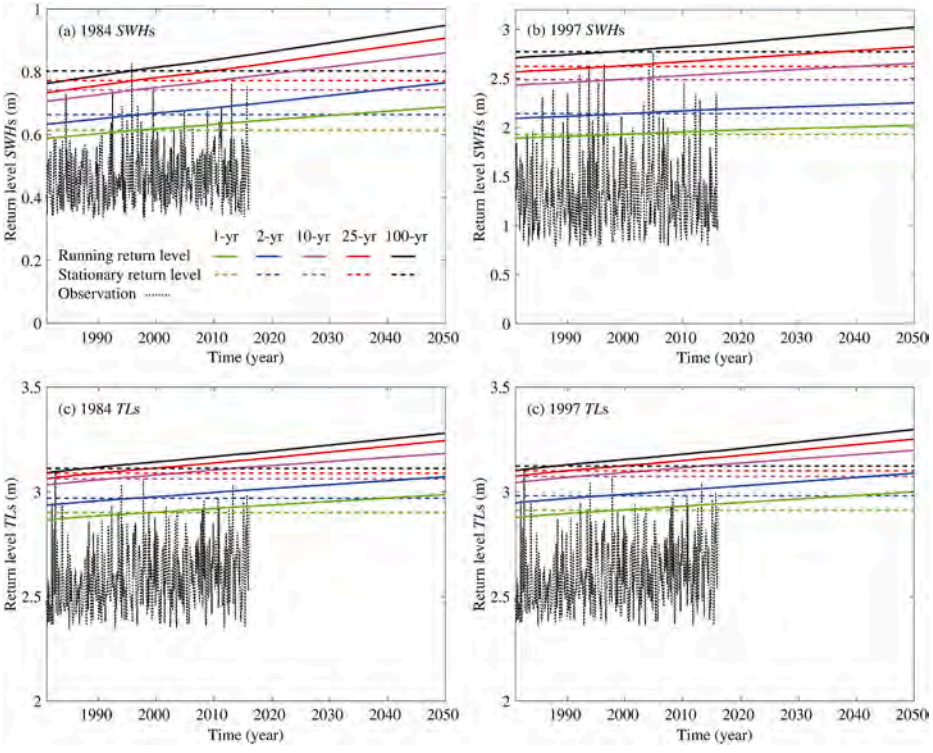

Fig. 13. Comparison of the running and stationary return levels before and after reclamation used for all years in coastal flood defense design.

Vuik et al., 2019), especially for Fengxian coastal area, where the foreshore has evolved from accumulating to eroding recently (Xie et al., 2017). Therefore, an assessment of sediment availability, technical feasibility, and long-term influence on landscape evolution is required before implementing the nature-based solution.

Although building with nature for flood protection is more challenging and effortful than seawall heightening (Vuik et al., 2016, 2018), the multiple benefits of flood mitigation and high ecological values could potentially be improved by designing hybrid foreshore-seawall systems via human foreshore restoration activities (Möller et al., 2014). This technique could be applied to other estuaries and coasts worldwide, especially for developing countries of emerging economies heavily dependent on intertidal reclamations (Temmerman et al., 2013; Barbier, 2015). Examples of the potential applications are the Pearl River Delta in China, the Ganges Delta in Bangladesh, the Manila Estuary Delta in the Philippines, and the Mekong Delta in Vietnam, where the low-lying deltas are vulnerable to typhoon impacts, thus the hybrid solution is more attractive.

6. Conclusions

With coastal reclamations, tidal flats are lost, while wave run-ups at the toe of the seawall are increased, threatening the sustainability of coastal development around Shanghai. As a safety measure to protect against flooding, seawall management requires a derivation of the quantitative relationship between tidal flat loss and the increase in extreme events intensity. The results show that the intertidal reclamations are the primary source of increased flood risks in locations dominated by wind waves, with both wind speed and wind direction being the essential driving factors. In particular, wind waves pose the highest flood hazard when wind speeds are the most extreme, and the wind direction is normal to the coastline. While reclamation and embankments have protected against extreme tidal water levels and storm surges of moderate severity on the Fengxian Coast, they have exacerbated more serious the wave run-ups of the seawall, and promote potential severe wave overtopping disasters when coincidence with the extreme storm surges. Tidal flat reclamation, therefore, aggravates the risk from storms and increases the frequency of occurrence of a given rate. It is concluded that the disasters of coastal flooding after the reclamation of 1997 in Hangzhou Bay are a result of both anthropogenic and natural activities.

The construction of the seawall-foreshore hybrid system is more sustainable and cost-effective than the conventional hard engineering defense. Although the practice of conventional defense design is well established, and few natural systems can eliminate all risks, these environmental approaches could potentially make a meaningful contribution. Where this function exists, its wave mitigation ability could be customized to enhance flood defense by the integration with conventional approaches, maximizing the system's contribution to flood protection. Understanding the effect of tidal flats on coastal protection under storm conditions is of utmost importance to determine the design criteria for hybrid flood defense systems of a seawall shielded by sufficient tidal flats as suggested by our proposed *ECF* relationship. This equivalent conversion relationship on flood protection may be relevant to other storm-impacted coastlines worldwide that are subject to large-scale reclamations.

Author statement

All authors contributed to the design and development of the work. The numerical experiments were originally carried out by Huayang Cai. Zhijun Dai and Jiahong Wen carried out the data analysis. Min Zhang built the model and wrote the manuscript. Tjeerd J. Bouma, Jeremy Bricker, Ian Townend and Tongtiegang Zhao reviewed and revised the manuscript.

Declaration of competing interest

The authors declare that they have no known competing financial interests or personal relationships that could have appeared to influence the work reported in this paper.

Acknowledgments

This research is supported by the National Natural Science Foundation of China (Project no.: 41701001, 2018YFE0109900, 51761135024), China Postdoctoral Science Foundation (Project no.: 2018M630414) and Guangdong Provincial Department of Science and Technology (2019ZT08G090). The authors would like to thank Dr. Elisa Ragno and Prof. Oswaldo Morales Napoles from Delft University of Technology for their helps on non-stationary Copulas. Great thanks are due to the reviewers for a number of very constructive comments and suggestions that have helped the substantial improvement of the manuscript.

Appendix A. Supplementary data

Supplementary data to this article can be found online at https://doi.org/10.1016/j.coastaleng.2021.103868.

References

Adnan, M.S.G., Haque, A., Hall, J.W., 2019. Have coastal embankments reduced flooding in Bangladesh? Sci. Total Environ. 682, 405–416.
Altomare, C., Suzuki, T., Chen, X., Verwaest, T., Kortenhaus, A., 2016. Wave overtopping of sea dikes with very shallow foreshores. Coast. Eng. 116, 236–257.
Barbier, E.B., 2015. Climate change impacts on rural poverty in low-elevation coastal zones. Estuar. Coast Shelf Sci. 165, A1–A13.
Bi, X., Liu, F., Pan, X., 2012. Coastal projects in China: from reclamation to restoration. Environ. Sci. Technol. 46 (9), 4691–4692.
Bouma, T.J., van Belzen, J., Balke, T., Zhu, Z., Airoldi, L., Blight, A.J., Davies, A.J., Galvan, C., Hawkins, S.J., Hoggart, S.P.G., Lara, J.L., Losada, I.J., Maza, M., Ondiviela, B., Skov, M.W., Strain, E.M., Thompson, R.C., Yang, S., Zanuttigh, B., Zhang, L., Herman, P.M.J., 2014. Identifying knowledge gaps hampering application of intertidal habitats in coastal protection: opportunities & steps to take. Coast. Eng. 87, 147–157.
Bouma, T.J., Vries, M.B.D., Low, E., Kusters, L., Herman, P.M.J., Tánczos, I.C., Temmerman, S., Hesselink, A., Meire, P., Regenmortel, S.V., 2005. Flow hydrodynamics on a mudflat and in salt marsh vegetation: identifying general relationships for habitat characterisations. Hydrobiologia 540 (1), 259–274.
Bouma, T.J., Vries, M.B.D., Herman, P.M.J., 2010. Comparing ecosystem engineering efficiency of two plant species with contrasting growth strategies. Ecology 91 (9), 2696–2704.
Cheng, L., AghaKouchak, A., Gilleland, E., Katz, R.W., 2014. Non-stationary extreme value analysis in a changing climate. Climatic Change 127 (2), 353–369.
Chini, N., Stansby, P.K., 2012. Extreme values of coastal wave overtopping accounting for climate change and sea level rise. Coast. Eng. 65, 27–37.
Dee, D.P., Uppala, S.M., Simmons, A.J., Berrisford, P., Poli, P., Kobayashi, S., Andrae, U., Balmaseda, M.A., Balsamo, G., Bauer, P., Bechtold, P., Beljaars, A.C.M., van de Berg, L., Bidlot, J., Bormann, N., Delsol, C., Dragani, R., Fuentes, M., Geer, A.J., Haimberger, L., Healy, S.B., Hersbach, H., Hólm, E.V., Isaksen, L., Kållberg, P., Köhler, M., Matricardi, M., McNally, A.P., Monge-Sanz, B.M., Morcrette, J.J., Park, B.K., Peubey, C., de Rosnay, P., Tavolato, C., Thépaut, J.N., Vitart, F., 2011. The ERA-Interim reanalysis: configuration and performance of the data assimilation system. Q. J. R. Meteorol. Soc. 137 (656), 553–597.
EDF, R.D.S., 2011. TOMAWAC software for sea state modelling on unstructured grids over oceans and coastal seas. EDF R&D. Release 6.1. France.
EurOtop, 2018. Manual on Wave Overtopping of Sea Defences and Related Structures: an Overtopping Manual Largely Based on European Research, but for Worldwide Application. http://www.overtopping-manual.com/eurotop/downloads/.
Janin, J.M., Lepeintre, F., Péchon, P., 1992. TELEMAC-3D: A Finite Element Code to Solve 3D Free Surface Flow Problems. Springer, pp. 489–506.
Kirwan, M.L., Temmerman, S., Skeehan, E.E., Guntenspergen, G.R., Fagherazzi, S., 2016. Overestimation of marsh vulnerability to sea level rise. Nat. Clim. Change 6, 253.
Kundzewicz, Z.W., Su, B., Wang, Y., Xia, J., Huang, J., Jiang, T., 2019. Flood risk and its reduction in China. Adv. Water Resour. 130, 37–45.
Lin-Ye, J., García-León, M., Gràcia, V., Ortego, M.I., Lionello, P., Sánchez-Arcilla, A., 2017. Multivariate statistical modelling of future marine storms. Appl. Ocean Res. 65, 192–205.
Lin-Ye, J., Garcia-Leon, M., Gracia, V., Sanchez-Arcilla, A., 2016. A multivariate statistical model of extreme events: an application to the Catalan coast. Coast. Eng. 117, 138–156.

Liu, X., Wang, Y., Costanza, R., Kubiszewski, I., Xu, N., Yuan, M., Geng, R., 2019. The value of China's coastal wetlands and seawalls for storm protection. Ecosyst. Serv. 36, 100905.
Loder, N.M., Irish, J.L., Cialone, M.A., Wamsley, T.V., 2009. Sensitivity of hurricane surge to morphological parameters of coastal wetlands. Estuar. Coast Shelf Sci. 84 (4), 625–636.
Méndez, F.J., Menéndez, M., Luceño, A., Losada, I.J., 2006. Estimation of the long-term variability of extreme significant wave height using a time-dependent Peak over Threshold (POT) model. J. Geophys. Res.: Oceans 111, C07024.
Menéndez, P., Losada, I.J., Beck, M.W., Torres-Ortega, S., Espejo, A., Narayan, S., Díaz-Simal, P., Lange, G., 2018. Valuing the protection services of mangroves at national scale: the Philippines. Ecosyst. Serv. 34, 24–36.
Möller, I., Kudella, M., Rupprecht, F., Spencer, T., Paul, M., van Wesenbeeck, B.K., Wolters, G., Jensen, K., Bouma, T.J., Miranda-Lange, M., Schimmels, S., 2014. Wave attenuation over coastal salt marshes under storm surge conditions. Nat. Geosci. 7 (10), 727–731.
Möller, I., Spencer, T., French, J.R., Leggett, D.J., Dixon, M., 1999. Wave transformation over salt marshes: a field and numerical modelling study from north Norfolk, England. Estuarine. Coast. Shelf Sci. 49 (3), 411–426.
Niroomandi, A., Ma, G., Ye, X., Lou, S., Xue, P., 2018. Extreme value analysis of wave climate in Chesapeake Bay. Ocean Eng. 159, 22–36.
Reed, D., van Wesenbeeck, B., Herman, P.M.J., Meselhe, E., 2018. Tidal flat-wetland systems as flood defenses: understanding biogeomorphic controls. Estuar. Coast Shelf Sci. 213, 269–282.
Rigby, R.A., Stasinopoulos, D.M., 2005. Generalized additive models for location, scale and shape. J. Roy. Stat. Soc.: Ser. C (Appl. Stat.) 54 (3), 507–554.
Rootzén, H., Katz, R.W., 2013. Design life level: quantifying risk in a changing climate. Water Resour. Res. 49 (9), 5964–5972.
Salauddin, M., Pearson, J.M., 2019. Wave overtopping and toe scouring at a plain vertical seawall with shingle foreshore: a physical model study. Ocean Eng. 171, 286–299.
Shi, Y., Zhu, J., Xie, Z., Ji, Z., Jiang, Z., Yang, G., 2000. Prediction and prevention of the impacts of sea level rise on the Yangtze River Delta and its adjacent areas. Sci. China Earth Sci. 43 (4), 412–422.
Temmerman, S., Meire, P., Bouma, T.J., Herman, P.M.J., Ysebaert, T., De Vriend, H.J., 2013. Ecosystem-based coastal defence in the face of global change. Nature 504 (7478), 79–83.
Tuan, T.Q., Oumeraci, H., 2010. A numerical model of wave overtopping on seadikes. Coast. Eng. 57 (8), 757–772.
Vuik, V., Borsje, B.W., Willemsen, P.W.J.M., Jonkman, S.N., 2019. Salt marshes for flood risk reduction: quantifying long-term effectiveness and life-cycle costs. Ocean Coast Manag. 171, 96–110.
Vuik, V., Jonkman, S.N., Borsje, B.W., Suzuki, T., 2016. Nature-based flood protection: the efficiency of vegetated foreshores for reducing wave loads on coastal dikes. Coast. Eng. 116, 42–56.
Vuik, V., Suh Heo, H.Y., Zhu, Z., Borsje, B.W., Jonkman, S.N., 2018. Stem breakage of salt marsh vegetation under wave forcing: a field and model study. Estuar. Coast Shelf Sci. 200, 41–58.
Wang, J., Gao, W., Xu, S., Yu, L., 2012. Evaluation of the combined risk of sea level rise, land subsidence, and storm surges on the coastal areas of Shanghai, China. Climatic Change 115 (3–4), 537–558.
Wang, L., Zhang, M., Wen, J., Chong, Z., Ye, Q., Ke, Q., 2019. Simulation of extreme compound coastal flooding in Shanghai. Adv. Water Sci. 30 (4), 546–555.
Willemsen, P.W.J.M., Borsje, B.W., Vuik, V., Bouma, T.J., Hulscher, S.J.M.H., 2020. Field-based decadal wave attenuating capacity of combined tidal flats and salt marshes. Coast. Eng. 156, 103628.
Xie, D., Pan, C., Wu, X., Gao, S., Wang, Z.B., 2017. Local human activities overwhelm decreased sediment supply from the Changjiang River: continued rapid accumulation in the Hangzhou Bay-Qiantang Estuary system. Mar. Geol. 392, 66–77.
Zhang, M., Townend, I., Cai, H., He, J., Mei, X., 2018a. The influence of seasonal climate on the morphology of the mouth-bar in the Yangtze Estuary, China. Continent. Shelf Res. 153 (Suppl. C), 30–49.
Zhang, M., Townend, I., Zhou, Y., Wang, L., Dai, Z., 2019. An examination of estuary stability in response to human interventions in the South Branch of the Yangtze (Changjiang) estuary, China. Estuarine. Coast. Shelf Sci. 228, 106383.
Zhang, X., Zhang, Y., Zhu, L., Chi, W., Yang, Z., Wang, B., Lv, K., Wang, H., Lu, Z., 2018b. Spatial-temporal evolution of the eastern Nanhui mudflat in the Changjiang (Yangtze River) Estuary under intensified human activities. Geomorphology 309, 38–50.